The effect of powder oxidation on defect formation in laser additive manufacturing

Chu Lun Alex Leung[1,2], Sebastian Marussi[2,3], Michael Towrie[4], Robert C. Atwood[5], Philip J. Withers[3], Peter D. Lee[1,2*]

[1] Department of Mechanical Engineering, University College London, Torrington Place, London WC1E 7JE, UK

[2] Research Complex at Harwell, Rutherford Appleton Laboratory, Oxfordshire OX11 0FA, UK

[3] Henry Royce Institute, School of Materials, The University of Manchester, Oxford Rd, Manchester, M13 9PL, UK

[4] Central Laser Facility, Research Complex at Harwell, UK Research & Innovation - Science & Technology Facilities Council, Rutherford Appleton Laboratory, Oxfordshire OX11 0QX, UK

[5] Diamond Light Source Ltd, Harwell Science & Innovation Campus, Oxfordshire, OX11 0DE, UK

*corresponding author: peter.lee@ucl.ac.uk

Abstract

Understanding defect formation during laser additive manufacturing (LAM) of virgin, stored, and reused powders is crucial for the production of high quality additively manufactured parts. We investigate the effects of powder oxidation on the molten pool dynamics and defect formation during LAM. We compare virgin and oxidised Invar 36 powder under overhang and layer-by-layer build conditions using *in situ* and *operando* X-ray Imaging. The oxygen content of the oxidised powder was found to be *ca.* 6 times greater (0.343 wt.%) than the virgin powder (0.057 wt.%). During LAM, the powder oxide is entrained into the molten pool, altering the Marangoni convection from an inward centrifugal to an outward centripetal flow. We hypothesise that the oxide promotes pore nucleation, stabilisation, and growth. We observe that spatter occurs more frequently under overhang conditions compared to layer-by-layer conditions. Droplet spatter can be formed by indirect laser-driven gas expansion and by the laser-induced metal vapour at the melt surface. In layer-by-layer build conditions, laser re-melting reduces the pore size distribution and number density either by promoting gas release from keyholing or by inducing liquid flow, partially or completely filling pre-existing pores. We also observe that pores residing at the track surface can burst during laser re-melting, resulting in either

formation of droplet spatter and an open pore or healing of the pore via Marangoni flow. This study confirms that excessive oxygen in the powder feedstock may cause defect formation in LAM.

Keywords: Spatter, porosity, synchrotron radiography, X-ray imaging, additive manufacturing, powder bed fusion, selective laser melting

1. Introduction

Laser additive manufacturing (LAM) selectively fuses powder particles together using a focused laser beam, layer-by-layer, to build up complex 3D objects [1]. It offers great promise in aerospace, nuclear fusion, and energy storage applications [2]; however, the uptake of LAM technologies in these areas has been hindered by inconsistent part performance. Specifically, the mechanical [3,4]**,** thermal and electrical properties [5] of additive manufactured components have been lower than wrought components due to the accumulation of residual stresses [6] and the presence of defects, such as porosity [7,8], balling [9], and cracks [10].

Defect formation mechanisms are difficult to characterise due to the timescale of the laser-matter interaction (10^{-6}-10^{-3} s) [11]. Although computer simulations can provide some physical understanding of the additive manufacturing (AM) processes [12], they require experimental data for model validation and verification, especially with regards to the molten pool and defect dynamics. Some data can be collected using *in situ* monitoring devices installed on AM systems [13,14]. However, these devices are unable to reveal dynamic behaviour inside the molten pool or melt track (*e.g.,* the evolution of porosity and lack of fusion defect) while forming a single layer or multi-layer tracks. Zhao *et al.* [15] studied the molten pool dynamics and phase transformation inside a weld pool during laser powder bed fusion (LBPF) using synchrotron X-ray imaging and diffraction. Calta *et al.* [16] extended this observing pore formation and phase transformation during LBPF of a single layer track. Guo *et al.* [17] elucidated the dynamics of powder spatter during LBPF for a single layer track. Leung *et al.* [7,8] revealed and quantified defect and molten pool dynamics during LAM of single and dual-layer tracks across a wide range of overhang conditions. However, to date, there have been no *in situ* studies examining the molten pool and defect dynamics and other thermophysical phenomena taking place during LAM of virgin and oxidised powders.

Prior ex situ studies have shown that LAM of oxidised powder can induce defects, *e.g.* porosity and cracks [18–21], decrease the powder flowability resulting in poor powder packing density [22], reduce

the wettability of the molten pool resulting in balling [19,23], and increase the surface roughness of the part [18], impairing the overall mechanical properties [20,24]. Understanding the effects of oxygen (or oxide) in the powder feedstock on AM processes would help developing mitigation strategies to minimise defect generation when processing stored, reused and highly reactive powders, *e.g.* Al-, Mg- and Ti-based alloys. This is because the stored or reused powder can pick up oxygen from powder handling and the storage environment [22] while the highly reactive powders may oxidise during use. At present, it remains unclear how oxides affect the molten pool and defect dynamics and how they give rise to poor build quality.

Although there is a link between powder oxidation and defect formation, there are many hypotheses on the causes and formation of closed pores in AM, including 1) powder contamination [25], 2) coating defects [26,27], 3) the presence of carbon [28], hydrogen [29,30] and oxide inclusion [18] in the molten pool, 4) internal gas porosity from the powder [28,29,31], 5) keyhole collapse [32] and 6) gas entrapment during laser melting [33]. Furthermore, there are a few studies on the formation of irregular [8,18,28,34] and open pores [7,8,31]. Experiments are required to confirm the aforementioned mechanisms and to establish the conditions under which they are active.

Powder spatter [4,17,35,36] and droplet spatter [4,37] are two other common defects found in LAM. They influence the resultant porosity [3,31,38] and surface finish [3] of AM parts. They may also lead to powder bed contamination, improper powder spreading, and damage to the AM system. [4,39–41]

Powder spatter [4] contributes to powder denudation at the laser-matter interaction zone. [35] It is induced by the interactions between metal vapour and Bernoulli effect-driven gas flow, *i.e.* metal vapour-driven particle entrainment. [35,36] Bidare *et al.* [42] correlated the evolution of spatter with the direction of the metallic plume generated from LAM. Quo *et al.* [17] postulated that the amount of powder spatter increases with increasing environmental pressure and layer thickness in LBPF [7].

Droplet spatter can form when there is a molten pool instability due to local boiling or melt evaporation [31,43,44], accumulation of recoil pressure [4,36,45], combining with the melt flow acceleration by Marangoni convection, resulting in a stream of liquid ejecting in a vertical direction. [4,35,44–47] It can also be formed as individual powder spatter [36] or as powder agglomerates passing through the laser beam and melting [7,36].

Here, our aim is to find out how different levels of powder oxidation affect the AM process, including its impact on the melt pool dynamics and defect formation. To do this, we use *in situ* and operando synchrotron X-ray imaging to follow the LAM process in real time. We examine the effects of powder oxidation by studying LAM using virgin and oxidised (stored for *ca.* 1 year) Invar 36 powder feedstock. Our results reveal how the oxide reverses Marangoni flow, directly affecting how different types of defects form.

2. Experimental methods

2.1. Powder characterisation

The morphology and chemical composition of gas atomised (GA) virgin and oxidised Invar 36 powder (TLS Technik GmbH & Co. Spezialpulver KG, Germany) and a virgin GA Invar 36 powder (Goodfellow Inc., UK) were characterised by a JEOL JSM-6610LV SEM equipped with energy dispersive spectroscopy (EDS). The particle size distribution was extracted using SEM images and Image Processing Toolbox in MATLAB 2016a (The MathWorks Inc, USA). X-ray Diffraction (XRD) was performed on the Invar 36 powder (TLS Technik GmbH & Co. Spezialpulver KG, Germany) using a PANalytical X'Pert Pro MPD series automated spectrometer (Malvern Instruments, UK) with a $Cu_{K\alpha}$ radiation (λ =1.541Å) at 40kV and 40mA, a 2θ scanning range (degrees) from 10° to 100° with a step size of 0.03°, and a count rate of 50 s per step. After XRD, we performed phase identification in Profex [48]. The O, N, H, and moisture content of the virgin and oxidised Invar 36 powder was measured by an inert gas fusion infra-red absorption (IGF-IR) method (ONH836, Leco cooperation, USA). We performed the IGF-IR test on the Invar 36 powder (TLS Technik GmbH & Co. Spezialpulver KG, Germany) after second build (B2) and virgin Invar 36 powder (Goodfellow Inc., UK) as a reference powder. We performed 5 tests per powder condition and each test required 5 g of powder.

The chemical states of the virgin powder and oxidised powder were examined by X-ray photoelectron spectroscopy (XPS) analysis (Nexsa Surface Analysis System, Thermo Fisher Scientific Inc., USA). Both powders were characterised using a micro-focused monochromatic Al X-ray source (72 W) over an area of ca. 400 x 400 μm^2. The XPS survey was conducted at a pass energy of 200 eV with a step size of 0.1 eV and a dwell time at 10 ms. High-resolution scans were conducted at a pass energy of 40 eV with a step size of 0.1eV and a dwell time of 50 ms. Charge neutralisation of

the sample was achieved using a combination of low energy electrons and Ar^+ ions. The experiment was performed at an argon partial pressure of 10^{-8} Torr in the x–y scan mode at ion acceleration of 3 kV and ion beam current density of 1 μA mm^{-2}. Binding energies were referenced to adventitious carbon at 284.8 eV, with peak fitting undertaken using CasaXPS version 2.3.15 (Casa Software Ltd, UK). The multiple-peaks fitting for Fe 2p and Ni 2p high-resolution scans were assigned based on prior work from Biesinger *et al.* [49]. The overlayer thickness (oxides/hydroxide) is calculated based on the Strohmeier's equation [50]:

$$d = \left(\lambda_{avg}\right) sin\ \theta\ ln(\left(\frac{N_M \lambda_M (I_{oxide}+I_{hydroxide})}{N_{avg}\lambda_{avg} I_M}\right) + 1) \quad \text{Equation 1}$$

where θ is the photoelectron take-off angle, λ_{avg} and λ_M are the average inelastic mean free path (IMPF) of the oxides/hydroxide and metal, respectively. The IMPF values (λ) were either directly obtained or calculated based on TPP-2M equation in the NIST standard reference database 71 (version 1.2).[51] N_{avg} and N_M are the volume densities of the metal atoms in oxides/hydroxide and metal, respectively. I_{oxide}, $I_{hydroxide}$, and I_M are the area percentages of the oxides, hydroxide and metal from the high-resolution spectrum, respectively.

2.2. In situ and *operando* LAM with synchrotron X-ray imaging

To reveal the effects of powder oxide on the fluid dynamic behaviour during LAM, we compare the additive manufacture using the same Invar 36 powder in two conditions, firstly in as-supplied (low oxide condition) and secondly after storage for *ca.* 1 year (high oxide condition). Using a LAM process replicator (LAMPR) that can be accommodated on a synchrotron imaging beamline we perform an overhang AM build on each powder condition (for details of the LAMPR see ref [7]). In each build, the LAM process was monitored by *operando* synchrotron X-ray radiography in the Beamline I12: Joint Engineering, Environmental, and Processing (JEEP) at Diamond Light Source [52].

A laser beam (wavelength 1030 - 1070 nm, transverse mode TEM_{00} - the first subscript stands for the radial mode and the second subscript stands for the angular mode of the laser beam) [11] and continuous-wave) scanned a 5 mm line at a power of 150 W and a nominal scan velocity of 5 mm s^{-1} across the Invar 36 powder bed (20 mm length, 0.3 mm wide and 3 mm deep) in an argon atmosphere at a flow rate of 4 l min^{-1}. A slow scan speed (v) of 5 mm s^{-1} was chosen to ensure continuous track formation under overhang conditions.

For the first AM build (B1), we performed LAM of a single layer track (B1.1) using a virgin Invar 36 powder with a 3 mm thick powder layer (for details see previous study [7]). The Invar 36 powder (TLS Technik GmbH & Co. Spezialpulver KG, Germany) was then kept in a container and exposed to air for *ca.* one year to simulate prolonged powder storage effects, allowing powder oxidation. A second single layer track AM build (B2.1) was produced *ca.* one year after B1 using the oxidised Invar 36 powder under precisely the same experimental conditions as B1. In addition, we laid down second (B2.2) and third (B2.3) layer melt tracks above the previous melt track while performing X-ray imaging to investigate the track-to-track interaction during LAM of the oxidised powder. In this study, the powder was manually spread above the substrate and melt tracks without lowering the substrate, therefore the layer thickness varied depending on how the prior melt track was formed. For B2, the layer thickness was ca. 3000 µm, 670 ± 420 µm, and 410 ± 170 µm for B1.1, B2.2, and B2.3, receptively.

All experiments were captured by synchrotron X-ray radiography at 5100 frames per second (fps) using 55 keV monochromatic X-rays, custom module optics with a 700 µm thick LuAg: Ce scintillator coupled with a Miro 310M camera (Vision Research, USA). Using a region of interest mode, the field of view (FOV) of the camera was 8.4 mm in width and 3.3 mm in height with a 6.6 µm pixel size. The image acquisition system was synchronised with the LAMPR using a ring buffer mode that continuously recorded images into the on-board memory of the camera. Once the laser was triggered, twelve thousand radiographs were recorded. For each experiment, we also captured one hundred dark-field images and one hundred flat-field images for flat field correction. [7]

2.3. Post-mortem X-ray computed tomography (XCT)

After the *in situ* and *operando* radiography experiments, the samples made by virgin (B1) and oxidised (B2) powders were examined by X-ray computed tomography (XCT) (Nikon XTH 225 X-ray microfocus tomography system, Nikon, Japan), see details in **Table 1**. The radiographic projections were reconstructed into a 16-bit image volume of 2000 x 2000 x 2000 voxels using the built-in beam hardening correction and filtered back projection algorithms in CT Pro3D (Nikon, Japan).

Table 1: XCT acquisition parameters for the imaging of Invar 36 melt tracks.

Sample	Accelerating voltage (kV)	Beam current (μA)	Number of projections	Exposure time (ms)	Scan volume (mm^3)	Voxel size (μm^3)
B1	100	100	1200	500	7.2^3	3.6
B2	100	100	3142	500	4.8^3	2.4

2.4. Image processing and quantification

The acquired synchrotron radiographs were post-processed and analysed using MATLAB 2016a. They were normalized by flat field correction [53] to remove image artefacts. A denoising algorithm, VBM3D [54], was applied, followed by background subtraction and segmentation. We quantified the spatter size and morphology, melt track geometry (*e.g.,* length and depth), and internal porosity over time (see details in [7,8]). The spatter velocity was quantified using segmented images and an imageJ [55] plugin - TrackMate [56].

3. Results and discussion

The particle size distribution of the oxidised powder is 5 – 70 μm with a mode of 10 μm (**Figure 1**). The Inset SEM image shows the powder surface before B2 is covered with oxides (**Figure 1a**), however, it exhibits a similar morphology and shape of the virgin powder before B1 (see details in ref [7]). The XRD pattern (**Figure 1b**) is consistent with the expected face centred cubic γ-(Fe, Ni) phase. According to the Invar 36 phase diagram [57], *α*-(Fe, Ni) phase can be formed below 353°C [57] but it was not detected by XRD. Qiu *et al.* [58] suggested that the volume fraction of *α*-(Fe, Ni) phase is below the detection limit of laboratory XRD instruments. Elmer *et al.* [59] showed rapid solidification can reduce solute redistribution, resulting in a single-phase alloy. This mechanism may also apply to LAM of Invar 36, inhibiting the formation of *α*- (Fe, Ni) phase.

Given that the penetration depth of EDS is < 5 μm, the oxygen results are mainly associated with the oxide layer at the powder surfaces, therefore we removed the oxygen content and normalised the Ni and Fe contents. The EDS analysis (**Table 2**) indicate the virgin and oxidised Invar 36 powders exhibit a similar ratio of Fe and Ni content. The IGF-IR analysis (**Table 2**) was used to obtain the oxygen

content from the bulk powder composition, revealing that the virgin powder (Goodfellow Inc., UK) exhibited 6 times less oxygen than the oxidised powder due to a reduced oxide layer.

Table 2: Elemental composition of the Invar 36 powder measured by EDS and IGF-IR. The EDS results were normalised, showing a ratio of Fe and Ni content.

Characterisation method	**EDS**		**IGF-IR**			
Powder sample #	**Fe (wt.%)**	**Ni (wt.%)**	**O (vol. %)**	**N (vol. %)**	**H (vol. %)**	**Moisture (ppm)**
Virgin (B1) - TLS Technik GmbH & Co. Spezialpulver KG	69 ± 0.4	31 ± 0.4	-	-	-	-
Oxidised (B2) - TLS Technik GmbH & Co. Spezialpulver KG, Germany	71 ± 1.3	29 ± 1.3	0.343	0.666	5.84×10^{-3}	11.6
Virgin (Reference) - Goodfellow Inc., UK	72 ± 0.1	28 ± 0.1	0.057	0.095	9.15×10^{-4}	35.9

The influence of powder surface chemistry on the molten pool dynamics is not well understood, therefore we have examined the powder surface of the virgin (reference) and oxidised invar 36 powders using XPS. **Figure 2** displays high-resolution scans of Ni 2p, Fe 2p, O 1s, and C 1s from both powder samples, showing the presence of Fe, Ni, FeO, Fe_2O_3, NiO, $Ni(OH)_2$, and adventitious carbon contaminations.

From the high-resolution XPS scans of Ni (**Figure 2a** and **e**) and Fe (**Figure 2b** and **f**), the shape and the peak area percentages of metal, metal oxides, and metal hydroxides are very similar. This suggests metal oxides/hydroxide are readily formed during powder processing, including during powder packaging and powder transfer. During LAM, the metal hydroxide most likely will thermally decompose to metal oxide and then release into the melt pool. The presence of iron oxides [60] and nickel oxide [61] in the molten pool can alter its temperature coefficient of surface tension from negative to positive, leading to the reversal of the Marangoni convection, generating centripetal convection. [62]

Using the O 1s spectra (**Figure 2c** and **g**) and the Strohmeier's equation [50], we have estimated the thickness of metal oxides and hydroxide on both powder surfaces, *i.e.* the overlayer thickness, see **Table 3**. Unexpectedly, the overlayer of the oxidised powder is only marginally thicker than that of the virgin powder (0.5 nm, or 5% in 12 nm total). Although not captured by XPS, the reference virgin powder

has a higher moisture content (**Table 2**) and formed a thick overlayer of NiO and $Ni(OH)_2$ at its surface. This may explain why the total overlayer thickness is similar to the oxidised powder.

The C 1s spectra (**Figure 2d** and **h**) also display a very similar peak shape. The total carbon contamination on the virgin and oxidised powders are 49 at.% and 17 at.%, respectively. Based on the area percentage of C 1s spectra and using the method depicted in ref. [63] the oxygen associated with the carbon species in virgin and oxidised powders were determined as 6 at.% and 15 at.%, respectively. During LAM, the carbon contaminants (containing oxygen) may either evaporate at elevated temperature or dissociate into oxygen and carbon in the molten pool. The oxygen may react with the molten Fe/Ni and form metal oxides, restricting the melt flow and promoting pore growth.

Table 3: Calculated thickness of iron oxides, nickel oxides, and nickel hydroxides

Powder type	Layer thickness (nm)				
	FeO	**Fe_2O_3**	**NiO**	**$Ni(OH)_2$**	**Total**
Virgin powder	1.3	7.1	1.3	2.1	11.8
Oxidised powder	1.4	8.0	1.1	1.8	12.3

3.1. LAM of virgin and oxidised Invar 36 powder

The initial, middle and final stages of the melt track evolution for the virgin powder (B1.1) are shown in **Figure 3a** (and complemented by **Supplementary video 1**). A high power density laser beam (10^6 W cm^{-2}) fuses the Invar 36 powder particles to form a molten pool and subsequently vaporises the top surface of the molten pool to form a metal vapour jet [17,35,36]. We postulate that the metal vapour jet indirectly heats the argon gas in the laser-matter interaction zone, both effects promote powder entrainment into the molten pool, spatter, and track growth. When the laser beam moves faster than the growth rate of the molten pool, it produces a separate molten pool ahead of the melt track. The Marangoni-driven flow and wetting move the newly formed molten pool behind the laser beam. The newly formed molten pool then merges with the melt track. [7,8] The aforementioned track formation mechanisms are summarised as molten pool wetting [7,8] and vapour-driven powder entrainment [7,36]. No pores are evident during melt track extension but spatter continues to eject from the powder bed in the same scan direction of the laser beam and argon gas flow. [7,41] Detailed quantification of the molten pool geometry and porosity during LAM is discussed in section 3.4.

Figure *3* Figure 3b and **Supplementary video 2** show the evolution of a first layer melt track for the oxidised powder (B2.1). This forms by similar mechanisms to those depicted for the virgin powder build (B1.1), however, there is extensive porosity in the first layer melt track using oxidised powder (B2.1) compared to virgin powder. In the first layer melt track with oxidised powder, the droplet spatter ahead of the scanning laser beam rotates in a clockwise direction (**Figure 3b**, **Supplementary Figure 1** and **Supplementary video 3**). However, the pores behind the scanning laser beam move anti-clockwise (**Figure 3c**), demonstrating the liquid metal in the molten pool flows radially outwards, *i.e.* centripetal Marangoni convection (**Supplementary videos 2** and **3**). This is contrary to what has been reported to the LAM of virgin powder study [7].

Most molten metals or alloys, including Fe-Ni alloys [64,65], have a negative temperature coefficient of surface tension. During LAM, the flow of the liquid metal is driven by the centrifugal Marangoni convection, sweeping the hotter and lower surface tension melt outwards to reduce the interfacial energy of the colder and higher surface tension melt. However, some studies report that when the oxygen concentration [O] in the molten pool is above 50 ppm, it is sufficient to alter the temperature coefficient of surface tension from negative to positive thereby changing the Marangoni convection from centrifugal to centripetal (see schematic in **Supplementary Figure 2** and **Supplementary video 3**).[62,66] **Table 2** shows that the [O] of the oxidised Invar 36 powder is at 3430 ppm, *ca.* 6 times higher than the reference virgin Invar 36 powder. This is significantly higher than the oxygen level required for centripetal Marangoni convection.

During LAM of oxidised powder, we observe two types of pores are present in the melt track: type I – gas pores and type II – pores surrounded by oxide layers. Type I gas pores have an equivalent diameter less than 250 μm, a low solubility and a high buoyancy in the melt fluid (**Figure 3c**). They usually form near the laser beam and reside adjacent to the melt track surface owing to the Marangoni flow. During LAM of the oxidised powder, the Marangoni flow entrains type I gas pores to different locations inside the melt track via centripetal Marangoni convection. Meanwhile, some coalescence occurs forming larger pores and some escape into the atmosphere via a keyhole (similar observations are reported in electron beam welding [67]). Leung *et al.* [7] observed that pore bursting promotes gas release from the melt track; however, the underlying mechanism remains unclear.

The size of the type II pores varies from 50 - 500 µm. Type II pores usually float *ca.* 200 µm behind the laser beam and reside near the melt track surface. These pores remain stationary throughout LAM, except for during pore growth. It is evident that the large type II pores grow at the expense of type I pores via Ostwald ripening, resulting in a final pore size of at least 350 µm, see examples in **Figure 3d**.

3.2. Spatter evolution mechanisms

From the single layer melt track experiments using virgin and oxidised powder, we observed both powder ejection and droplet spatter throughout LAM. Our results show that the laser-melt track interaction creates a laser-induced vapour jet and a recoil pressure normal to the melt track surface, ejecting powder while creating a denudation zone (**Figure 3**, **Figure 4** and **Supplementary video 3**). We speculate that the denudation zone is in an inverse bell shape and it contains a high concentration of metal vapour (**Figure 4a**). [42] The high-temperature metal vapour indirectly heats the surrounding argon gas, creating a convection or inward argon flow within the denuded zone, promoting vapour-driven powder entrainment for melt track extension [7,35,36].

During the overhang build, the melt track extends deeper into the powder bed while expanding in the horizontal direction, because the powder particles near the melt track are removed by the combination of metal vapour and hot argon gas. The laser beam melts the powder deeper into the powder bed and ahead of the melt track (**Figure 4a**), reducing the growth rate of the melt track as it extends. The laser beam continues to move, it eventually irradiates onto the powder ahead of the melt track and forming a new molten bead (**Figure 4b**). Sometimes, the laser beam moves ahead of the first melt bead, forming another bead whilst growing the first bead, because the laser beam profile is sufficiently broad to interact with both melt beads and the powder between the two beads. The laser beam may create a sufficiently strong vapour plume at the surface of the first bead (**Figure 4b – marker 1**), ejecting these new smaller metal beads (**Figure 4b – marker 2**) from the laser-matter interaction zone as droplet spatter, see examples in **Supplementary video 3**). These observations are evident in both virgin and oxidised powder cases, highlighting the difficultly of producing overhang features in LAM.

We have quantified the spatter size and velocity during LAM of virgin and oxidised powders, and also analysed the spatter behaviour over three different spatter size categories: (I) one; (II) one to two; and (III) > two times the powder size distribution. **Table 4** shows a similar spatter distribution in both

studies wherein a majority of spatter is 1 to 2 times the particle size distribution. The oxidised powder study generates slightly more category III spatter (>132 μm) than the virgin powder study.

Figure 5a shows a positive correlation between the spatter size and velocity, although with a very large scatter. In both virgin and oxidised powder cases, most spatter has a velocity of 0.4 m s^{-1}, however, some spatter from the oxidised powder case has a velocity in the range of 0.4 – 0.9 m s^{-1}. In general, the spatter velocity in both cases matches prior studies. [7,8]

Figure 5b illustrates the different spatter morphologies during LAM. With virgin powder, the spatter is roughly spherical across all size categories. With oxidised powder, the category I and II spatters are irregularly shaped and formed from agglomerated powder. It appears that the coarsening into spherical droplets is hindered, illustrating the oxides are either chemically and/or physically different. Category III spatter primarily consists of droplet spatter with its surface covered by agglomerated powder. The evidence clearly shows powder oxidation strongly affects powder agglomeration, pore formation, and pore stabilisation [68].

Table 4: Spatter tracking results for AM of virgin and oxidised powders

Size category	Spatter types	Size range (μm)	Normalised frequency (%)	
			Virgin powder	Oxidised powder
I	Powder spatter	$D_{eq} \leq 73$	3 %	4 %
II	Powder spatter/cluster + droplet spatter	$73 < D_{eq} \leq 132$	81 %	72 %
III	Droplet spatter	$D_{eq} > 132$	16 %	23 %

3.3. The roles of molten pool dynamics on pore bursting

In the virgin powder study, pore bursting is not evident under the processing conditions used in this study. However, Leung et al. [7] demonstrated that pore bursting occurs during solidification via pore coalescence and pore migration.

In the oxidised powder study, we have revealed a different pore bursting mechanism during LAM of the second layer melt track (B2.2) as shown in **Figure 6** and **Supplementary video 4**. The laser beam forms a keyhole, penetrating through the second powder layer and re-melting the top surface of the first layer melt track (**Figure 6a** and **Supplementary video 5**). Laser re-melting promotes pore transport in the molten pool, allowing gas pores to escape into the atmosphere through a keyhole, similar observations are shown in the first layer melt track (B2.1) and **Figure 3b**. For gas entrainment

316 to take place, these gas pores must locate *ca.* 1 mm from the powder bed surface (based on our setup).
317 Below this depth, laser re-melting can only generate a small amount of liquid metal that partially fills the
318 pre-existing pores by liquid feeding (green dotted circles in **Figure 6a**). We speculate that the oxide
319 films at the pore surface may act as a physical barrier, combined with the adventitious carbon
320 contaminations, altering the interfacial energy in the molten pool, restricting the melt flow that normally
321 entrains or eliminates pores. Our observations support and validate the mechanisms proposed by
322 previous work [18,21].

323 **Figure 6b** uncovers a new mechanism of open pore formation during LAM. At 7 ms, the laser re-
324 melts the surface of first layer melt track and forms a liquid bridge (indicated by purple dotted lines).
325 Between 10 and 34.8 ms, the laser beam causes the liquid bridge to double its size while accelerating
326 its internal melt flow, which promotes pore coalescence, growth, and transport. By 34.8 ms, the
327 Marangoni-driven flow entrains gas pores towards both ends of the liquid bridge, significantly weakening
328 its structural integrity. The laser beam raises the temperature of the material surrounding the pore,
329 heating the gas pore (see red dotted arrows) and expanding the volume of the gas pore proportionally.
330 Once the gas pressure exceeds the surface tension of the liquid bridge, the liquid bridge ruptures (35
331 ms) and ejects vertically as a stream of liquid metal (36 ms), forming droplet spatter. Consequently, the
332 closed pore burst opens, leaving a dent or crater (also known as an open pore [7,31,69]) at the melt
333 track surface.

334 Based on our observations, there is no visible laser re-melting feature at the bottom of the pore until
335 40 ms (orange dotted circle in **Figure 6**). This indicates that the droplet spatter is ejected before the
336 formation of an open pore, and hence metal vaporisation did not contribute to the formation of droplet
337 spatter and open pores, an additional mechanism to prior hypotheses [35,36,42].

338 Regarding the formation mechanism of open pores, Qiu *et al.* [69] hypothesised that they are formed
339 by insufficient liquid feeding; however, Leung *et al.* [7] revealed that open pores are formed by pore
340 bursting during solidification. Here, we show another formation mechanism of open pores, such that
341 pore bursting during laser melting, coupled with the formation of droplet spatter, resulting in an open
342 pore at the track surface.

343 **Figure 7** (complemented by **Supplementary video 6**) shows the evolution of a third layer melt track
344 (B2.3) in LAM of oxidised powder. Similar to the second layer melt track (B2.2), the laser beam melts

the powder above an open pore at the front of the melt track, forming a liquid bridge which temporarily closes the pore. As LAM progresses, the laser beam induces an indirect laser-driven gas expansion inside the pore which overcomes the strength of the liquid bridge, resulting in pore bursting, followed by the formation of an open pore and droplet spatter. This repeatable observation demonstrates pore bursting is a key formation mechanism of droplet spatter and open pores in LAM of oxidised powder and may apply to LAM of virgin powders. By 34 ms, the Marangoni convection causes the liquid metal to flow in the opposite direction of the scanning laser beam, showing one mechanism for pore closure. In the third layer build, laser re-melting removes many large pores in second layer melt track but also introduces many new type I pores. The oxide films at the pore surface are possibly disrupted, breaking into small pieces during laser re-melting [18]; however, they remain inside the molten pool, promoting nucleation and stabilisation of pores [70].

Figure 7b (and **Supplementary video 7**) reveals a new pore healing mechanism during LAM**.** The laser beam penetrates through the second and third layer melt tracks, opening a pre-existing pore (361 ms). The gas expands radially inside the pre-existing pore, pushing the liquid metal upwards (362 ms). Subsequently, the liquid metal driven by the high surface tension swirls back into the top track (indicated by dotted red arrows), healing the pore. The inward flow of liquid metal may be driven by Marangoni convection, combining with the weight of the liquid metal, causing the molten pool to swirl up and fall back down, healing the pore (361 – 363 ms).

Our results show that pore bursting can lead to either formation of droplet spatter resulting in an open pore (**Figure 6b**) or pore healing (**Figure 7b**). We postulate that the outcome of pore bursting depends on the size of the pre-existing pore before laser re-melting. In the third layer melt track, the diameter of the pre-existing pore is *ca.* 250 μm about 4 times smaller than the pore shown in the second layer build (**Figure 6b**). The gas pressure exerted from the pore in **Figure 7b** is expected to be lower than the one in **Figure 6b**. During laser re-melting, an interaction between the laser beam and a low gas pressure pore may lead to pore healing whereas the interaction between the laser beam and a high gas pressure pore may lead to the formation of droplet spatter. We also hypothesise that the position of the gas pores and the liquid bridge will affect the outcomes of pore bursting (see 34.8 ms in **Figure 6b**). However, a further study is required to determine whether there are a critical pore diameter and

position that lead to pore healing or formation of droplet spatter, resulting in open pore during laser re-melting.

3.4. Time-resolved quantification of molten pool geometry and porosity

Using the X-ray radiographs, we have quantified the changes in melt track geometry and its internal porosity throughout LAM, see **Figure 8.**

Figure 8a shows the track length for oxidised powder (L-B2.1) is ca. 20% greater than virgin powder (L-B1.1). This is due to 1) the reduced surface tension causes the molten pool to spread out further, and 2) the increased in spatter ahead of the laser beam, extending the track towards the bottom of the powder bed. The track depth in the oxidised powder study (D-B2.1) is twice of that in the virgin powder study (D-B1.1), because the reversal of Marangoni convection causes the liquid to flow inwardly from the centre to the bottom of the molten pool, advecting heat down to make a deeper pool while entraining gas pores. The entrained porosity increases the track volume and melt depth. [61]

Figure 8b quantifies porosity evolution during LAM. In the virgin powder study (blue), the molten pool/melt track continues to release gas bubbles in LAM as can be seen by the changes of greyscale in **Supplementary Video 8**. These gases are not retained in the melt track due to their low solubility, and thus the 2D porosity analysis shows the final porosity (Pore-B1.1) is 0.02%. From **Supplementary Video 8**, it is also evident that with virgin powder, the pores are driven to the surface by centrifugal Marangoni convection and then escape into the atmosphere.

In contrast, the melt track produced by the oxidised powder shows a large increase of porosity at the onset of the LAM (green), resulting in up to 24% final porosity (Pore-B2.1). The overlayer of oxide/hydroxide on the oxidised powder surfaces appears to have two strong effects on porosity. Firstly, this generates a centripetal Marangoni convection which drives any pre-existing pores to the bottom of the melt pool; secondly, the Marangoni convection deepens the melt pool and facilitates pore coalescence. Our results suggest the oxide stabilises the pores once formed, reduces the interfacial energy, and hence increases the pore size [71,72]. Given that the quantification algorithm does not take open pores into account, the sudden decrease of porosity in the second layer build (see event 1 in Pore-B2.2) indicates the formation of an open pore via pore bursting. In the third layer build, another drop in porosity (see event 2 in Pore-B2.3) denotes another pore bursting event has taken place. As

LAM progresses, the porosity gradually decreases from 24% to 18% because laser remelting allows gas porosity to escape from the keyhole at a penetration depth of < 1 mm.

3.5. Post-mortem 3D analysis

The pixel resolution of the synchrotron X-ray imaging setup is 6.6 µm per pixel, this implies we are unable to quantify any pores with a diameter less than approximately 20 µm [73], additionally, the radiographic analysis does not consider the pore depth along the X-ray beam path. Hence, we performed high-resolution XCT scans (with 2.4 x 2.4 x 2.4 μm^3 per voxel) to examine the samples made from virgin and oxidised powders, visualising and quantifying the morphology and pore size distributions in 3D. **Figure 9a** shows that the melt track produced from the virgin powder exhibits 0.08% porosity. Based on the resolution of the XCT data, the melt track shows no open pores but contains some closed pores with an area equivalent diameter (D_{eq}) of 10 µm. **Figure 9b** shows that the melt track produced from an oxidised powder has a total porosity of 15.1%, two-thirds of that (8.6%) is open pores and one-third of that (6.5%) is closed pores.

The largest closed pore in the sample made from virgin powder (B1) has a D_{eq} of 70 µm whereas the largest closed and open pores in the sample made from oxidised powder (B2) having a D_{eq} of 540 µm and 610 µm, respectively. The normalised frequency graphs (**Figure 9c**) show that both samples exhibit a significant amount of small pores with a D_{eq} of 10 µm. We postulate that they are type I gas pores due to their small size. In contrast, the cumulative frequency graphs (**Figure 9c**) show that there are fewer and larger pores in B2 sample than those in B1 sample, suggesting that the presence of oxide films in the molten pool promotes pore formation and possibly pore growth during LAM. These pores are potent crack initiator that deteriorates the fatigue resistance of AM parts when they are under cyclic loading.[74]

4. Conclusions

This study addresses the effects of powder oxidation on the molten pool dynamics and reveals new, evolution mechanisms of spatter, porosity and denuded zone during LAM of virgin and oxidised powders.

Three types of powders were characterised by SEM-EDS, IGF-IR, and XPS, including a virgin powder for B1, an oxidised powder for B2 (same powder used for B1 but kept for 1 year), and a

reference virgin powder. The oxidised powder shows an increasing of oxide layer thickness due to either oxygen pick up from powder handling and/or long-term storage under non-ideal conditions.

Our results confirm that molten pool wetting and vapour-driven powder entrainment are key track growth mechanisms for LAM. The oxygen content from the oxidised powder is sufficient to alter the temperature coefficient of the surface tension of the molten Invar 36 from negative to positive, altering the Marangoni convection from an outward centrifugal to inward centripetal flow. The oxides may act as nucleation sites for pore formation and subsequently stabilise these pores.

Two types of pores are revealed in the melt tracks: Type I gas pores have a diameter less than 250 μm, a low solubility, and a high buoyancy in the liquid metal whereas type II pores with a diameter greater than 250 μm can be formed by coalescing type I pores and also promoted by the presence of oxide film, stabilising the pore structure and restricting pore transport.

The powder surface chemistry is very complex and has impacts to powder agglomeration and defect formation. In the oxidised powder study, a significant amount of spatter is evident during LAM and some of which are covered by powder agglomerates, removing significant of powder in the powder bed.

Laser re-melting under layer-by-layer conditions may disrupt the oxide layers within the prior melt tracks, enabling gas pores to escape into the atmosphere via keyholing. It also reduces the size of pre-existing pores if these pores are located within the laser penetration depth of *ca.* 1 mm for the conditions studied. Otherwise, pores are partially filled by liquid feeding, changing them from a spherical to an irregular shape.

We uncover two new phenomena associated with pore bursting during LAM: (1) promoting pore healing by liquid feeding or (2) inducing open pores by the formation of droplet spatter. This demonstrates droplet spatter can be formed by indirect laser-driven gas expansion inside the melt track and by the laser-induced vapour jet at the melt surface.

The quantified results and the proposed mechanisms show defects in the additive manufacture can be minimised by using a low oxygen content metal powder. The new formation mechanisms of open pores and droplet spatter can enhance existing process simulation models to predict these defects. The quantification of melt track geometry over time can be used to calibrate the simulation model to

accurately predict the fluid flow behaviour during LAM. Lastly, the porosity quantification over time can be used to verify and enhance existing process simulation for defect prediction during layer-by-layer build conditions.

5. Acknowledgments

The authors acknowledge financial support from the EPSRC MAPP Future Manufacturing Hub (EP/P006566/1, www.mapp.ac.uk) and grants (EP/I02249X/1 and EP/M009688/1) and the AMAZE (Additive Manufacturing Aiming towards Zero Waste and Efficient Production of High-Tech Metal Products) project funded by the 7th Framework Programme of the European Commission (contract FP7-2012-NMP-ICT-FoF-313781). We acknowledge the use of facilities and support provided by the Research Complex at Harwell and thank Diamond Light Source for providing the beamtime (proposal numbers: EE13641-1 and EE16214-1) and staff (including Dr. Kazimir Wanelik) at beamline: I12 for their technical assistance. We thank the team members (particularly Drs. Anne-Laure Fauchille, Enyu Guo, Daniil Kazantsev, Sam Tammas-Williams, and Miss Lorna Sinclair) for their assistance in the beam times. We would also like to thank Mr. Xiaomeng Shi for his assistance for performing powder characterisation using XRD and LPW technology Ltd. for conducting the inert gas fusion infra-red (IGF-IR) absorption tests on the virgin and oxidised Invar 36 powders. PJW is grateful for funding from the ERC Advanced Grant (CORREL-CT Project ID: 695638). XPS data collection was performed at the EPSRC National Facility for XPS ('HarwellXPS'), operated by Drs Shaoliang Guan and Mark Isaacs. From Cardiff University and UCL under contract No. PR16195.

6. References

[1] J. Bonnin Roca, P. Vaishnav, E.R.H. Fuchs, M.G. Morgan, Policy needed for additive manufacturing, Nat. Mater. 15 (2016) 815–818. http://dx.doi.org/10.1038/nmat4658.

[2] T.M. Pollock, Alloy design for aircraft engines, Nat. Mater. 15 (2016) 809–815. http://dx.doi.org/10.1038/nmat4709.

[3] C. Qiu, S. Yue, N.J.E. Adkins, M. Ward, H. Hassanin, P.D. Lee, P.J. Withers, M.M. Attallah, Influence of processing conditions on strut structure and compressive properties of cellular lattice structures fabricated by selective laser melting, Mater. Sci. Eng. A. 628 (2015) 188–197. doi:10.1016/j.msea.2015.01.031.

[4] Y. Liu, Y. Yang, S. Mai, D. Wang, C. Song, Investigation into spatter behavior during selective laser melting of AISI 316L stainless steel powder, Mater. Des. 87 (2015) 797–806. doi:10.1016/j.matdes.2015.08.086.

[5] K.A. Ibrahim, B. Wu, N.P. Brandon, Electrical conductivity and porosity in stainless steel 316L scaffolds for electrochemical devices fabricated using selective laser sintering, Mater. Des. 106 (2016) 51–59. doi:10.1016/j.matdes.2016.05.096.

[6] M. Shiomi, K. Osakada, K. Nakamura, T. Yamashita, F. Abe, Residual stress within metallic model made by selective laser melting process, CIRP Ann. - Manuf. Technol. 53 (2004) 195–198. http://www.sciencedirect.com/science/article/pii/S0007850607606775.

[7] C.L.A. Leung, S. Marussi, R.C. Atwood, M. Towrie, P.J. Withers, P.D. Lee, In situ X-ray imaging of defect and molten pool dynamics in laser additive manufacturing, Nat. Commun. 9 (2018) 1355. doi:10.1038/s41467-018-03734-7.

[8] C.L.A. Leung, S. Marussi, M. Towrie, J. del Val Garcia, R.C. Atwood, A.J. Bodey, J.R. Jones, P.J. Withers, P.D. Lee, Laser-matter interactions in additive manufacturing of stainless steel SS316L and 13-93 bioactive glass revealed by in situ X-ray imaging, Addit. Manuf. (2018). doi:10.1016/J.ADDMA.2018.08.025.

[9] N.K. Tolochko, S.E. Mozzharov, I.A. Yadroitsev, T. Laoui, L. Froyen, V.I. Titov, M.B. Ignatiev, Balling processes during selective laser treatment of powders, Rapid Prototyp. J. 10 (2004) 78–87. doi:10.1108/13552540410526953.

[10] N.J. Harrison, I. Todd, K. Mumtaz, Reduction of micro-cracking in nickel superalloys processed by Selective Laser Melting: A fundamental alloy design approach, Acta Mater. 94 (2015) 59–68. doi:10.1016/j.actamat.2015.04.035.

[11] Steen, William; Jyotirmoy, Mazumder, Laser material processing, 4th ed., Springer-Verlag London, 1998. doi:10.1007/978-1-84996-062-5.

[12] M. Markl, C. Körner, Multiscale modeling of powder bed–based additive manufacturing, Annu. Rev. Mater. Res. 46 (2016) 93–123. doi:10.1146/annurev-matsci-070115-032158.

[13] S.K. Everton, M. Hirsch, P. Stravroulakis, R.K. Leach, A.T. Clare, Review of in-situ process monitoring and in-situ metrology for metal additive manufacturing, Mater. Des. 95 (2016) 431–445. doi:10.1016/j.matdes.2016.01.099.

[14] M. Mahesh, B. Lane, A. Donmez, S. Feng, S. Moylan, R. Fesperman, Measurement science needs for real-time control of additive manufacturing powder bed fusion processes, 2015. doi:dx.doi.org/10.6028/NIST.IR.8036.

[15] C. Zhao, K. Fezzaa, R.W. Cunningham, H. Wen, F. Carlo, L. Chen, A.D. Rollett, T. Sun, Real-time monitoring of laser powder bed fusion process using high-speed X-ray imaging and diffraction, Sci. Rep. 7 (2017) 3602.

[16] N.P. Calta, J. Wang, A.M. Kiss, A.A. Martin, P.J. Depond, G.M. Guss, V. Thampy, A.Y. Fong, J.N. Weker, K.H. Stone, C.J. Tassone, M.J. Kramer, M.F. Toney, A. Van Buuren, M.J. Matthews, An instrument for in situ time-resolved X-ray imaging and diffraction of laser powder bed fusion additive manufacturing processes, Rev. Sci. Instrum. 89 (2018) 055101. doi:10.1063/1.5017236.

[17] Q. Guo, C. Zhao, L.I. Escano, Z. Young, L. Xiong, K. Fezzaa, W. Everhart, B. Brown, T. Sun, L. Chen, Transient dynamics of powder spattering in laser powder bed fusion additive manufacturing process revealed by in-situ high-speed high-energy x-ray imaging, Acta Mater. 151 (2018) 169–180. doi:10.1016/j.actamat.2018.03.036.

[18] E. Louvis, P. Fox, C.J. Sutcliffe, Selective laser melting of aluminium components, J. Mater. Process. Tech. 211 (2011) 275–284. doi:10.1016/j.jmatprotec.2010.09.019.

[19] D. Gu, D. Dai, Role of melt behavior in modifying oxidation distribution using an interface incorporated model in selective laser melting of aluminum-based material, J. Appl. Phys. 120 (2016) 083104. doi:10.1063/1.4961410.

[20] E. Jelis, M. Clemente, S. Kerwien, N.M. Ravindra, M.R. Hespos, Metallurgical and Mechanical Evaluation of 4340 Steel Produced by Direct Metal Laser Sintering, JOM. 67 (2015) 582–589. doi:10.1007/s11837-014-1273-8.

[21] E.O. Olakanmi, R.F. Cochrane, K.W. Dalgarno, A review on selective laser sintering/melting

(SLS/SLM) of aluminium alloy powders: Processing, microstructure, and properties, Prog. Mater. Sci. 74 (2015) 401–477. doi:10.1016/j.pmatsci.2015.03.002.

[22] J.H. Tan, W.L.E. Wong, K.W. Dalgarno, An overview of powder granulometry on feedstock and part performance in the selective laser melting process, Addit. Manuf. 18 (2017) 228–255. doi:10.1016/J.ADDMA.2017.10.011.

[23] A. Simchi, H. Pohl, Effects of laser sintering processing parameters on the microstructure and densification of iron powder, Mater. Sci. Eng. A. 359 (2003) 119–128. doi:10.1016/S0921-5093(03)00341-1.

[24] W.A. Grell, E. Solis-Ramos, E. Clark, E. Lucon, E.J. Garboczi, P.K. Predecki, Z. Loftus, M. Kumosa, Effect of powder oxidation on the impact toughness of electron beam melting Ti-6Al-4V, Addit. Manuf. 17 (2017) 123–134. doi:10.1016/j.addma.2017.08.002.

[25] B.J. Dawes, R. Bowerman, Introduction to the Additive Manufacturing Powder Metallurgy Supply Chain Exploring the production and supply of metal powders for AM processes, Johnson Matthey Technol. Rev. 59 (2015) 243–256. doi:10.1595/205651315X688686.

[26] A.B. Spierings, N. Herres, G. Levy, Influence of the particle size distribution on surface quality and mechanical properties in AM steel parts, Rapid Prototyp. J. 17 (2011) 195–202. doi:10.1108/13552541111124770.

[27] F.J. Gürtler, M. Karg, M. Dobler, S. Kohl, I. Tzivilsky3, M. Schmidt, Influence of powder distribution on process stability in laser beam melting: Analysis of melt pool dynamics by numerical simulations, in: Solid Free. Symp. Texas, 2014: pp. 1099–1117.

[28] M. Rombouts, J.-P. Kruth, L. Froyen, P. Mercelis, P. Merce, Fundamentals of selective laser melting of alloyed steel powders, CIRP Ann. - Manuf. Technol. 55 (2006) 187–192. doi:http://dx.doi.org/10.1016/S0007-8506(07)60395-3.

[29] N.T. Aboulkhair, N.M. Everitt, I. Ashcroft, C. Tuck, Reducing porosity in AlSi10Mg parts processed by selective laser melting, Addit. Manuf. 1 (2014) 77–86. doi:10.1016/j.addma.2014.08.001.

[30] C. Weingarten, D. Buchbinder, N. Pirch, W. Meiners, K. Wissenbach, R. Poprawe, Formation and reduction of hydrogen porosity during selective laser melting of AlSi10Mg, J. Mater. Process. Technol. 221 (2015) 112–120. doi:10.1016/j.jmatprotec.2015.02.013.

[31] C. Qiu, C. Panwisawas, M. Ward, H.C. Basoalto, J.W. Brooks, M.M. Attallah, On the role of melt flow into the surface structure and porosity development during selective laser melting, Acta Mater. 96 (2015) 72–79. doi:10.1016/j.actamat.2015.06.004.

[32] H. Gong, D. Christiansen, J. Beuth, J.J. Lewandowski, Melt Pool Characterization for Selective Laser Melting of Ti-6Al-4V Pre-alloyed Powder, in: Solid Free. Fabr. Symp., 2014: pp. 256–267.

[33] F. Léonard, S. Tammas-williams, P.B. Prangnell, I. Todd, P.J. Withers, Assessment by X-ray CT of the effects of geometry and build direction on defects in titanium ALM parts, in: Conf. Ind. Comput. Tomogr., 2012: pp. 85–93. http://www.ndt.net/article/ctc2012/papers/91.pdf (accessed August 22, 2017).

[34] L. Thijs, J. Van Humbeeck, K. Kempen, E. Yasa, J.-P. Kruth, Investigation on the inclusions in maraging steel produced by Selective Laser Melting, in: 5th Int. Conf. Adv. Res. Virtual Rapid Prototyp., CRC Press, 2011: pp. 297–304. doi:doi:10.1201/b11341-48\r10.1201/b11341-48.

[35] M.J. Matthews, G. Guss, S.A. Khairallah, A.M. Rubenchik, P.J. Depond, W.E. King, Denudation of metal powder layers in laser powder bed fusion processes, Acta Mater. 114 (2016) 33–42. doi:10.1016/j.actamat.2016.05.017.

[36] S. Ly, A.M. Rubenchik, S.A. Khairallah, G. Guss, M.J. Matthews, Metal vapor micro-jet controls material redistribution in laser powder bed fusion additive manufacturing, Sci. Rep. 7

(2017) 4085. doi:10.1038/s41598-017-04237-z.

[37] D. Wang, S. Wu, F. Fu, S. Mai, Y. Yang, Y. Liu, C. Song, Mechanisms and characteristics of spatter generation in SLM processing and its effect on the properties, Mater. Des. 117 (2017) 121–130. doi:10.1016/j.matdes.2016.12.060.

[38] H. Nakamura, Y. Kawahito, K. Nishimoto, S. Katayama, Elucidation of melt flows and spatter formation mechanisms during high power laser welding of pure titanium, J. Laser Appl. 27 (2015) 032012. doi:10.2351/1.4922383.

[39] K. Mumtaz, N. Hopkinson, Selective laser melting of Inconel 625 using pulse shaping, Rapid Prototyp. J. 16 (2010) 248–257. doi:doi:10.1108/13552541011049261.

[40] M. Simonelli, C. Tuck, N.T. Aboulkhair, I. Maskery, I. Ashcroft, R.D. Wildman, R. Hague, A Study on the Laser Spatter and the Oxidation Reactions During Selective Laser Melting of 316L Stainless Steel, Al-Si10-Mg, and Ti-6Al-4V, Metall. Mater. Trans. A. 46 (2015) 3842–3851. doi:10.1007/s11661-015-2882-8.

[41] A. Bin Anwar, Q. Pham, Effect of inert gas flow velocity and unidirectional scanning on the formation and accumulation of spattered powder during selective laser melting, Proc. 2nd Int. Conf. Prog. Addit. Manuf. (Pro-AM 2016). (2016).

[42] P. Bidare, I. Bitharas, R.M. Ward, M.M. Attallah, A.J. Moore, Fluid and particle dynamics in laser powder bed fusion, Acta Mater. 142 (2018) 107–120. doi:10.1016/j.actamat.2017.09.051.

[43] W.E. King, H.D. Barth, V.M. Castillo, G.F. Gallegos, J.W. Gibbs, D.E. Hahn, C. Kamath, A.M. Rubenchik, Observation of keyhole-mode laser melting in laser powder-bed fusion additive manufacturing, J. Mater. Process. Technol. 214 (2014) 2915–2925. doi:10.1016/j.jmatprotec.2014.06.005.

[44] S.A. Khairallah, A.T. Anderson, A. Rubenchik, W.E. King, Laser powder-bed fusion additive manufacturing: Physics of complex melt flow and formation mechanisms of pores, spatter, and denudation zones, Acta Mater. 108 (2016) 36–45. doi:10.1016/j.actamat.2016.02.014.

[45] A.F.H. Kaplan, J. Powell, Spatter in laser welding, J. Laser Appl. 23 (2011) 032005. doi:10.2351/1.3597830.

[46] V. V. Semak, J.A. Hopkins, M.H. McCay, T.D. McCay, Melt pool dynamics during laser welding, J. Phys. D. Appl. Phys. 28 (1999) 2443–2450. doi:10.1088/0022-3727/28/12/008.

[47] A. Heider, J. Sollinger, F. Abt, M. Boley, R. Weber, T. Graf, High-speed X-ray analysis of spatter formation in laser welding of copper, in: Phys. Procedia, 2013: pp. 112–118. doi:10.1016/j.phpro.2013.03.058.

[48] N. Doebelin, R. Kleeberg, Profex: A graphical user interface for the Rietveld refinement program BGMN, J. Appl. Crystallogr. 48 (2015) 1573–1580. doi:10.1107/S1600576715014685.

[49] M.C. Biesinger, B.P. Payne, A.P. Grosvenor, L.W.M. Lau, A.R. Gerson, R.S.C. Smart, Resolving surface chemical states in XPS analysis of first row transition metals, oxides and hydroxides: Cr, Mn, Fe, Co and Ni, Appl. Surf. Sci. 257 (2011) 2717–2730. doi:10.1016/J.APSUSC.2010.10.051.

[50] B.R. Strohmeier, An ESCA method for determining the oxide thickness on aluminum alloys, Surf. Interface Anal. 15 (1990) 51–56. doi:10.1002/sia.740150109.

[51] C.J. Powell, A. Jablonski, F. Salvat, NIST Databases With Electron Elastic-Scattering Cross Sections, Inelastic Mean Free Paths, and Effective Attenuation Lengths, Surf. Interface Anal. 37 (2005). https://www.nist.gov/publications/nist-databases-electron-elastic-scattering-cross-sections-inelastic-mean-free-paths-and (accessed November 3, 2018).

[52] M. Drakopoulos, T. Connolley, C. Reinhard, R. Atwood, O. Magdysyuk, N. Vo, M. Hart, L.

631 Connor, B. Humphreys, G. Howell, S. Davies, T. Hill, G. Wilkin, U. Pedersen, A. Foster, N. De
632 Maio, M. Basham, F. Yuan, K. Wanelik, I12: the Joint Engineering, Environment and
633 Processing (JEEP) beamline at Diamond Light Source, J. Synchrotron Radiat. 22 (2015) 828–
634 838. doi:10.1107/S1600577515003513.

635 [53] V. Van Nieuwenhove, J. De Beenhouwer, F. De Carlo, L. Mancini, F. Marone, J. Sijbers,
636 Dynamic intensity normalization using eigen flat fields in X-ray imaging, Opt. Express. 23
637 (2015) 27975. doi:10.1364/OE.23.027975.

638 [54] K. Dabov, A. Foi, V. Katkovnik, Image denoising by sparse 3D transformation-domain
639 collaborative filtering, IEEE Trans. Image Process. 16 (2007) 1–16.
640 doi:10.1109/TIP.2007.901238.

641 [55] C. Schneider, W.S. Rasband, K.W. Eliceiri, NIH Image to ImageJ: 25 years of image analysis,
642 Nat. Methods. 9 (2012) 671–675. doi:10.1038/nmeth.2089.

643 [56] J.-Y. Tinevez, N. Perry, J. Schindelin, G.M. Hoopes, G.D. Reynolds, E. Laplantine, S.Y.
644 Bednarek, S.L. Shorte, K.W. Eliceiri, TrackMate: An open and extensible platform for single-
645 particle tracking, Methods. 115 (2017) 80–90. doi:10.1016/j.ymeth.2016.09.016.

646 [57] I.. V. Vernyhora, E. Al., Thermodynamics of f.c.c.-Ni–Fe Alloys in a Static Applied Magnetic
647 Field, ISRN Thermodyn. 212 (2012) 917836. doi:10.5402/2012/917836.

648 [58] C. Qiu, N.J.E. Adkins, M.M. Attallah, Selective laser melting of Invar 36: Microstructure and
649 properties, Acta Mater. 103 (2016) 382–395. doi:10.1016/j.actamat.2015.10.020.

650 [59] J.W. Elmer, T.W. Eagar, S.M. Allen, Single-Phase Solidification During Rapid-Resolidification
651 of Stainless Steel Alloys, Proc. Mater. Weldability Symp. Mater. Week, Detroit, MI. 3 (1990)
652 143–150.
653 http://citeseerx.ist.psu.edu/viewdoc/download?doi=10.1.1.666.1759&rep=rep1&type=pdf
654 (accessed May 2, 2018).

655 [60] S.-P. Lu, H. Fujii, K. Nogi, Weld shape comparison with iron oxide flux and Ar–O_2 shielding
656 gas in gas tungsten arc welding, Sci. Technol. Weld. Join. 9 (2004) 272–276.
657 doi:10.1179/136217104225012346.

658 [61] S. Lu, H. Fujii, H. Sugiyama, M. Tanaka, K. Nogi, Weld Penetration and Marangoni Convection
659 with Oxide Fluxes in GTA Welding, Mater. Trans. 43 (2002) 2926–2931.
660 doi:10.2320/matertrans.43.2926.

661 [62] K.C. Mills, B.J. Keene, R.F. Brooks, A. Shirali, Marangoni effects in welding, Philos. Trans. R.
662 Soc. A Math. Phys. Eng. Sci. 356 (1998) 911–925. doi:10.1098/rsta.1998.0196.

663 [63] B.P. Payne, M.C. Biesinger, N.S. McIntyre, X-ray photoelectron spectroscopy studies of
664 reactions on chromium metal and chromium oxide surfaces, J. Electron Spectros. Relat.
665 Phenomena. 184 (2011) 29–37. doi:10.1016/J.ELSPEC.2010.12.001.

666 [64] A. Sharan, A. Cramb, Surface tension and wettability studies of liquid Fe-Ni-O alloys, Metall.
667 Mater. Trans. B. 28 (1997) 465–472. doi:10.1007/s11663-997-0113-4.

668 [65] J. Brillo, I. Egry, Surface tension of nickel, copper, iron and their binary alloys, J. Mater. Sci. 40
669 (2005) 2213–2216. doi:10.1007/s10853-005-1935-6.

670 [66] C.X. Zhao, C. Kwakernaak, Y. Pan, I.M. Richardson, Z. Saldi, S. Kenjeres, C.R. Kleijn, The
671 effect of oxygen on transitional Marangoni flow in laser spot welding, Acta Mater. 58 (2010)
672 6345–6357. doi:10.1016/j.actamat.2010.07.056.

673 [67] R.C.R. Jianglin Huang, Richard Turner, Jean-Christophe Gebelin, Nils Warnken, Martin
674 Strangwood, The Effect of Hydrogen on Porosity Formation during Electron Beam Welding of
675 Titanium Alloys, Trends Weld. Res. 2012 Proc. 9th Int. Conf. (ASM Int. (2012) 868–875.

676 [68] J. Tientong, S. Garcia, C.R. Thurber, T.D. Golden, Synthesis of Nickel and Nickel Hydroxide

Nanopowders by Simplified Chemical Reduction, J. Nanotechnol. 2014 (2014) 1–6. doi:10.1155/2014/193162.

[69] C. Qiu, N.J.E. Adkins, M.M. Attallah, Microstructure and tensile properties of selectively laser-melted and of HIPed laser-melted Ti–6Al–4V, Mater. Sci. Eng. A. 578 (2013) 230–239. https://www.sciencedirect.com/science/article/pii/S0921509313005017?via%3Dihub#f0030 (accessed May 2, 2017).

[70] P.D. Lee, A. Chirazi, D. See, Modeling microporosity in aluminum-silicon alloys: A review, J. Light Met. 1 (2001) 15–30. doi:10.1016/S1471-5317(00)00003-1.

[71] R.C. Atwood, P.D. Lee, A three-phase model of hydrogen pore formation during the equiaxed dendritic solidification of aluminum-silicon alloys, Metall. Mater. Trans. B. 33 (2002) 209–221. doi:10.1007/s11663-002-0006-5.

[72] E. Guo, S. Shuai, D. Kazantsev, S. Karagadde, A.B. Phillion, T. Jing, W. Li, P.D. Lee, The influence of nanoparticles on dendritic grain growth in Mg alloys, Acta Mater. 152 (2018) 127–137. doi:10.1016/J.ACTAMAT.2018.04.023.

[73] E. Maire, P.J. Withers, Quantitative X-ray tomography, Int. Mater. Rev. 59 (2014) 1–43. doi:10.1179/1743280413Y.0000000023.

[74] G. Kasperovich, J. Hausmann, Improvement of fatigue resistance and ductility of TiAl6V4 processed by selective laser melting, J. Mater. Process. Technol. 220 (2015) 202–214. doi:10.1016/j.jmatprotec.2015.01.025.

Author contributions

PDL and CLAL conceived the project. CLAL, SM, and MT led the *in situ* additive manufacturing replicator and laser design. CLAL designed and performed all experiments, with all authors contributing. CLAL performed the data analysis. CLAL, PDL and PJW led the results interpretation and paper writing, with all authors contributing.

Data Availability

Representative samples of the research data are given in the figures (and supplementary data – DOI if available). Other datasets generated and/or analysed during this study are not publicly available due to their large size but are available from the corresponding author on reasonable request.

Competing interests

The authors declare no competing financial interests.

Figure captions

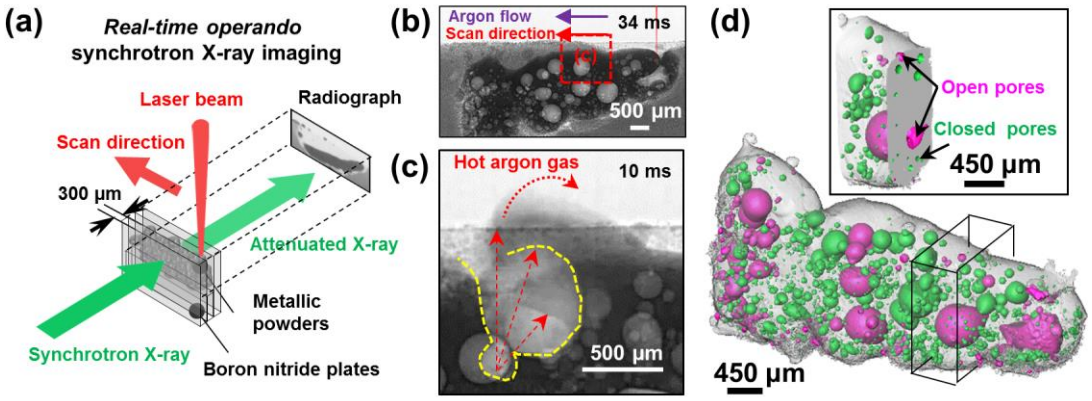

Graphical abstract: Using a laser additive manufacturing process replicator with *in situ* and *operando* X-ray imaging (a) permits capturing the formation of (b) porosity and (c) spatter during laser-matter interaction. In addition, we performed post mortem X-ray computed tomography analysis (d) reveal two types of pores inside the melt track: (i) open pores and (ii) closed pores.

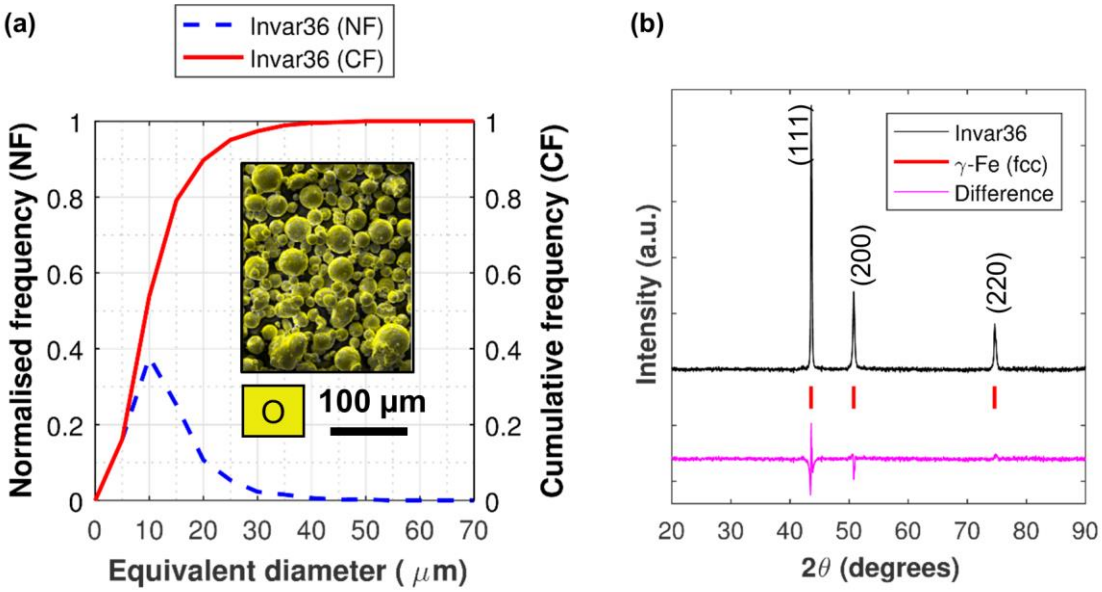

Figure 1: Powder characterisation of Invar 36: (a) particle size distribution. Inset: oxygen EDS map overlaid on a SEM secondary electron image. (b) XRD pattern showing the presence of *γ*-phase.

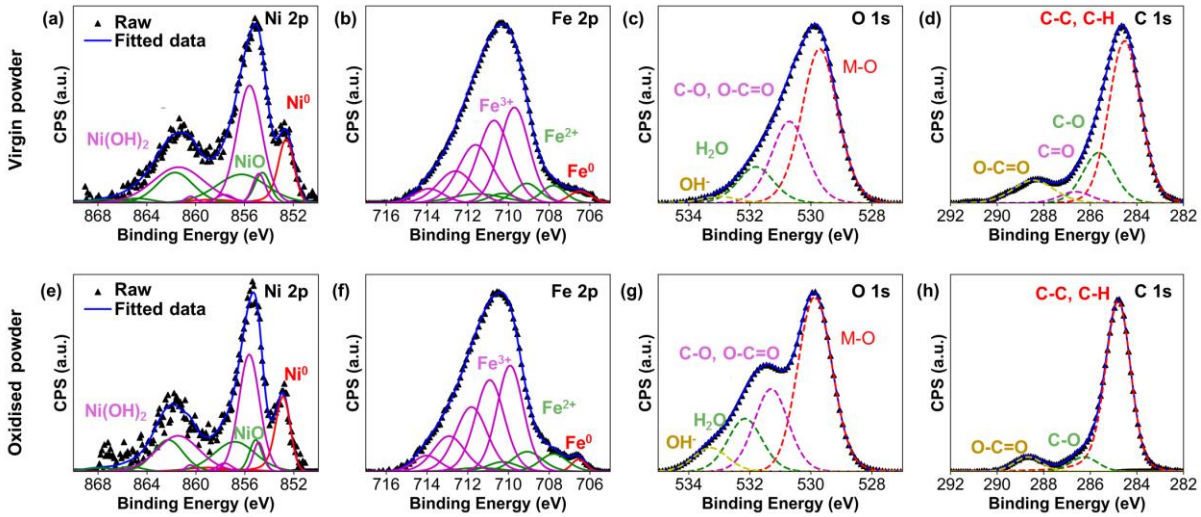

719

720 **Figure 2:** XPS spectra of (a-d) virgin, and (e-h) oxidised Invar 36 powders. The high-resolution spectra

721 are: (a, e) Ni 2p, (b, f) Fe 2p, (c, g) O 1s, and (d, h) C 1s.

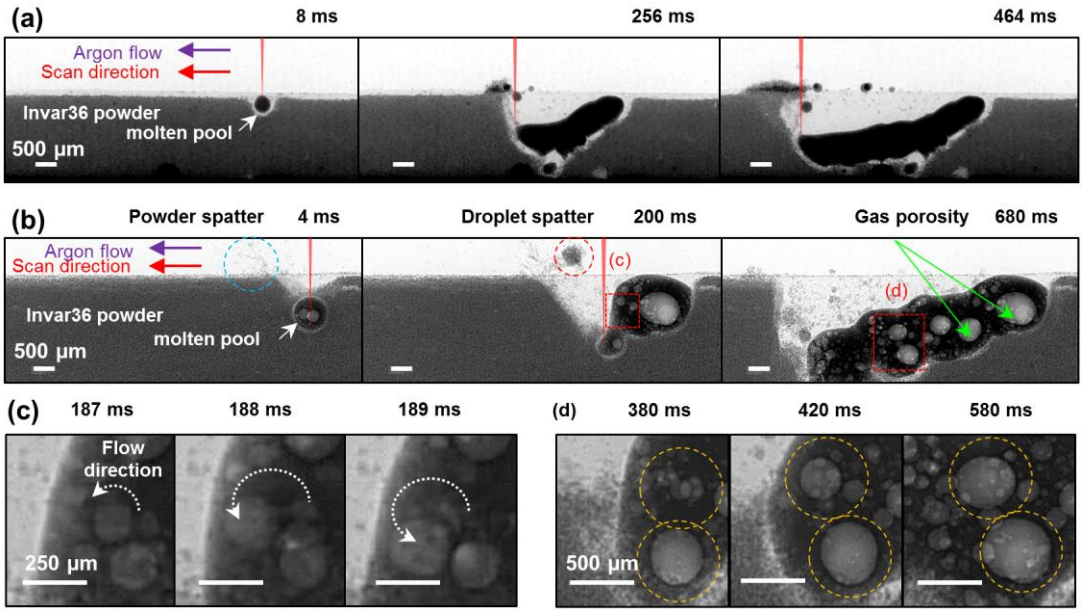

722

723 **Figure 3:** Times-series radiographs showing melt features observed during LAM of the first layer Invar

724 36 melt track (P = 150 W and v = 5 mm s^{-1}) for (a) a virgin powder to form B1.1 (**supplementary video**

725 **1**) and (b) a oxidised (stored for ca. 1 year) powder to form B2.1 (**supplementary video 2**). Blue circle:

726 powder spatter; red circle: molten spatter. The zoomed regions of interest (and **supplementary video**

727 **3**) in (b) two distinct pore evolution mechanisms are observed and shown in more detail in (c) pore

728 coalescence and migration by the centripetal Marangoni convection (white arrows) and (d) pore growth

729 promoted by oxide films (see orange circles).

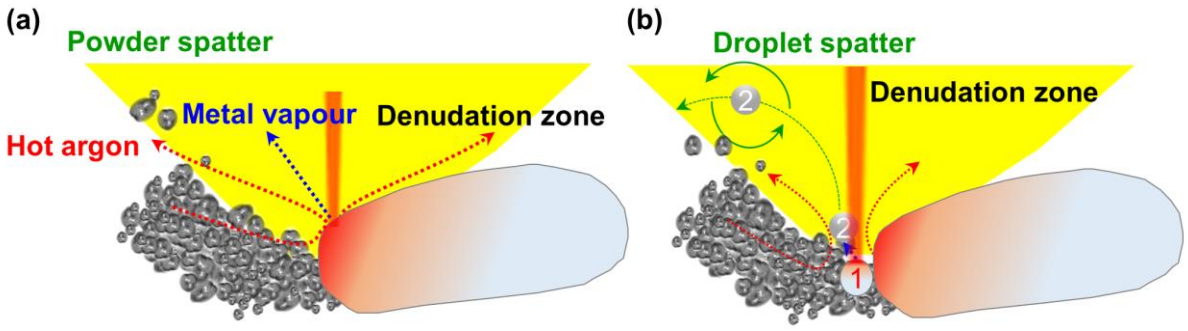

730

731 **Figure 4:** Schematic showing the effect of laser beam position in the melt track on spatter evolution: (a)
732 formation of powder spatter when laser beam positioned on the melt track and (b) formation of droplet
733 spatter when the laser beam is positioned ahead of the melt track.

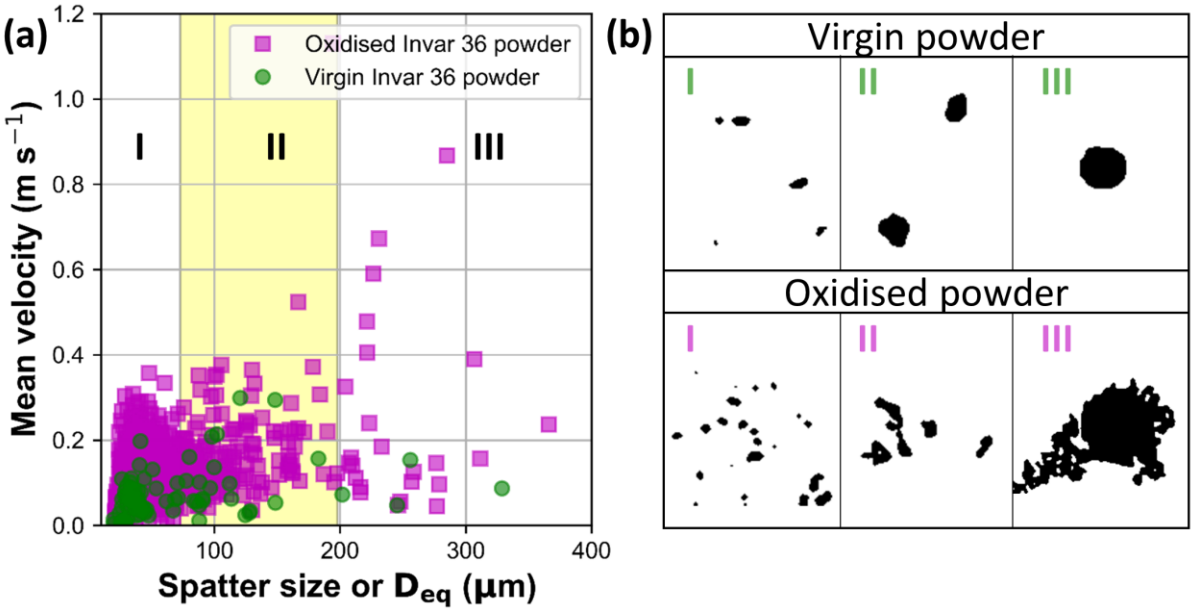

734

735 **Figure 5:** Spatter analysis for LAM of virgin and oxidised powder, divided into three categories: I.
736 powder spatter only; II. powder spatter/agglomeration + droplet spatter; III. droplet spatter only. (a)
737 Spatter size and velocity, and (b) spatter morphology for each category.

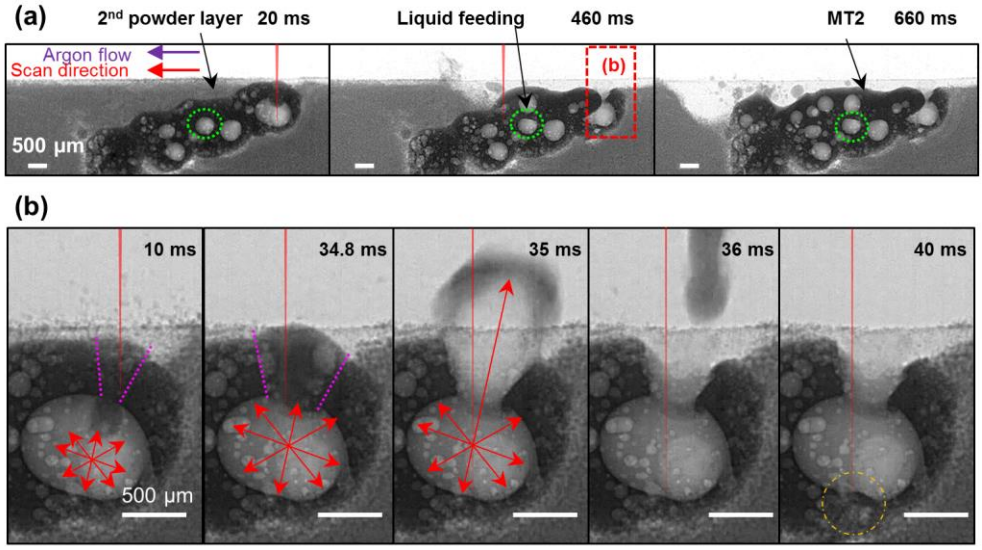

738

739 **Figure 6:** Times-series radiographs (complemented by **supplementary video 4**) showing a second
740 layer Invar 36 melt track (B2.2) with oxidised powder (P = 150 W and v = 5 mm s^{-1}). (a) Snapshots of
741 LAM at t = 20, 460, and 680 ms. The red box highlights a region of interest (ROI). (b) The ROI reveals
742 a new pore formation mechanism, where the expanded gas ejected the liquid bridge as droplet spatter
743 (35 - 36 ms), leaving an open pore behind (40 ms) (see **supplementary video 5)**. Red arrows indicate
744 gas expansion. Purple dotted lines highlight the liquid bridge region. Orange dotted circles highlight
745 laser re-melting at the bottom of the open pore after spattering.

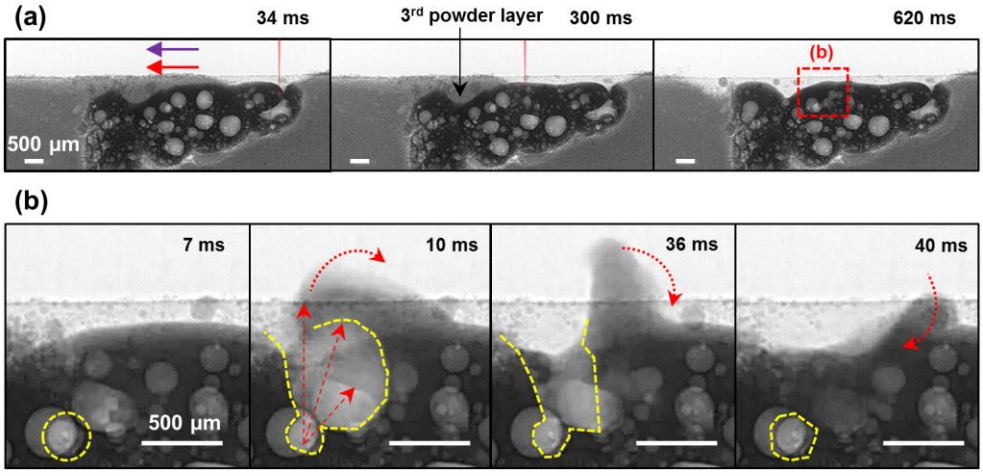

746

747 **Figure 7**: Times-series radiographs (and **Supplementary video 6**) showing LAM of a third layer Invar
748 36 melt track (B2.3) by a power of 150 W and a scan velocity of 5 mm s^{-1}. (a) Snapshots of the LAM
749 process at time t = 34, 300 and 620 ms. **(b)** The ROI and **Supplementary video 7** reveal a pore healing
750 mechanism, whereby the high surface tension of the molten pool inhibits spatter ejection, falling back
751 to heal the pore.

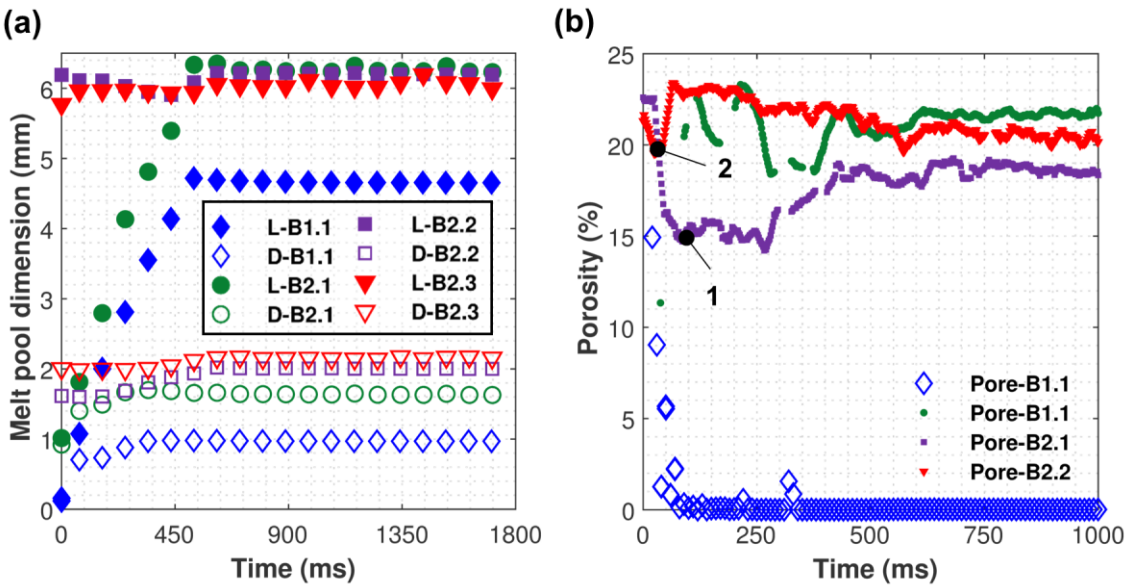

752

753 **Figure 8:** Quantification of melt features in B2: (a) length and depth of the first (B2.1), second (B2.2),

754 and third (B2.3) layer melt tracks and (b) the changes of porosity in each melt track over time.

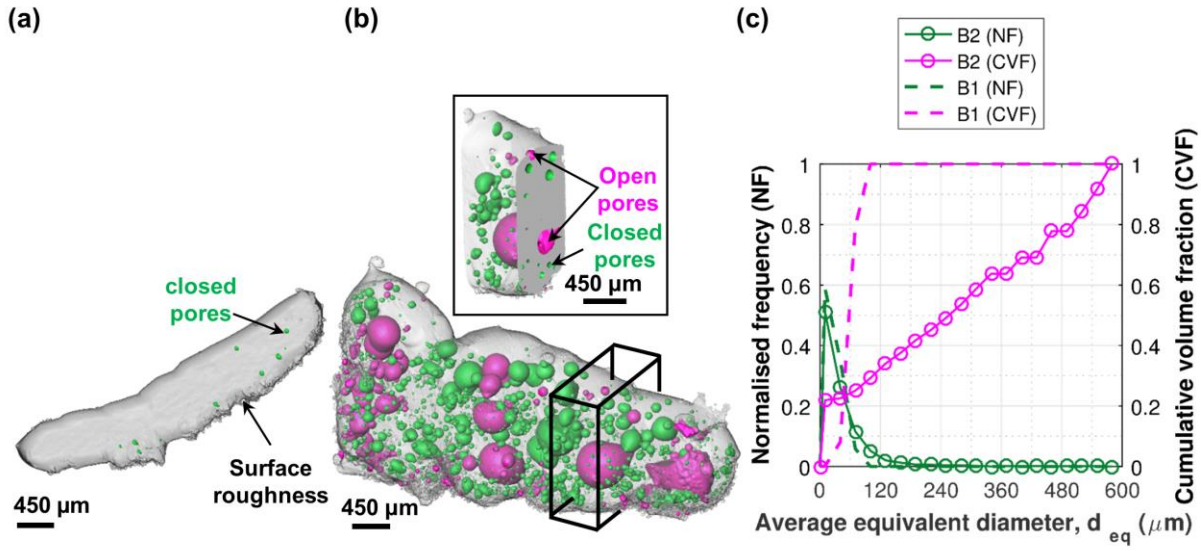

755

756 **Figure 9:** 3D volume rendering of melt tracks made from (a) virgin powder (B1) and (b) oxidised powder

757 (B2). (c) Their corresponding pore size distributions.

758

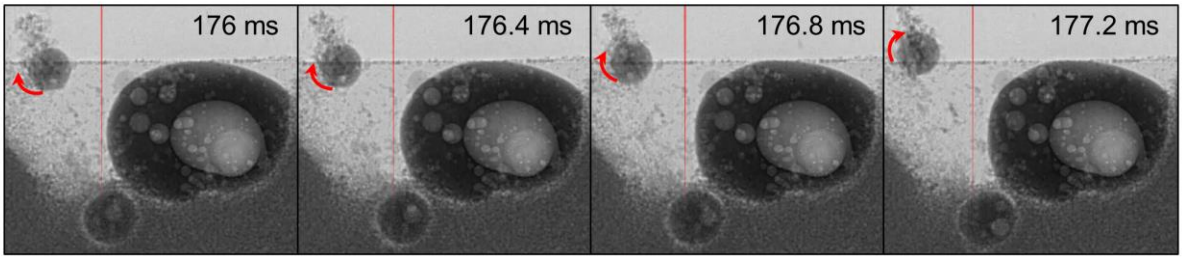

Supplementary Figure 1: Droplet spatter is ejecting upwards while rotating in the clockwise direction. The red line indicates the position of the laser beam as it moves from right to left.

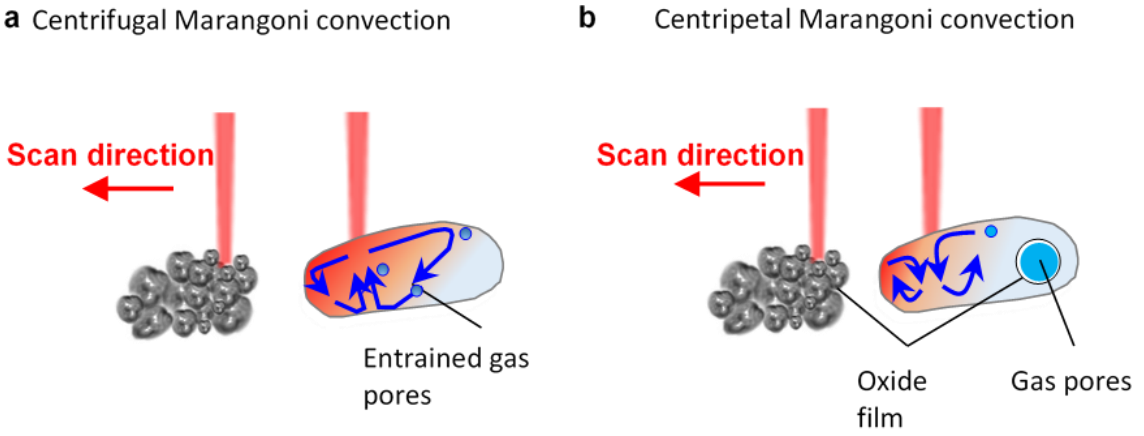

Supplementary Figure 2: Schematic of Marangoni convection during LAM of (a) virgin powder and (b) oxidised powder. (a) Melt fluid with a negative temperature dependent surface tension coefficient shows gas entrainment and (b) the oxide alters the flow direction, restricts the melt flow area and promotes pore growth.

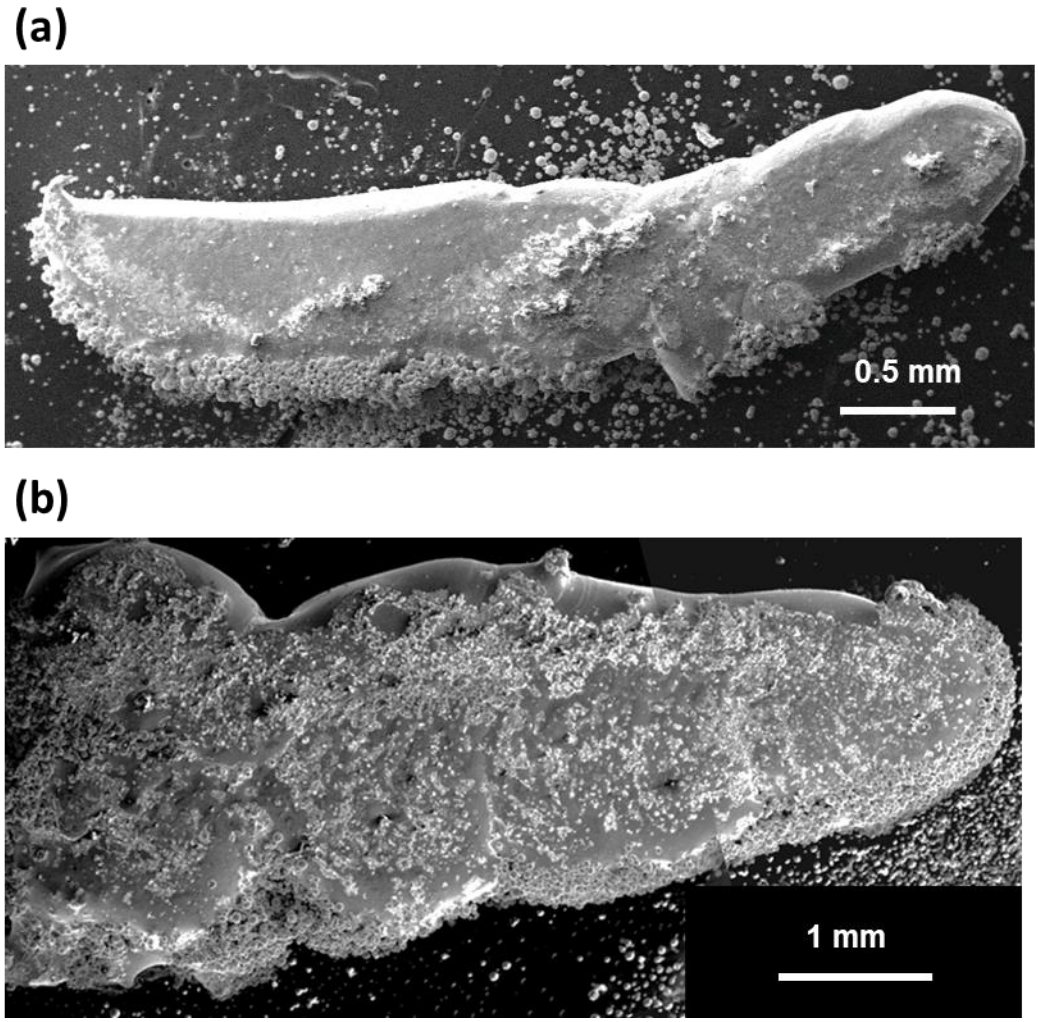

Supplementary Figure 3: (a) Secondary electron images showing the melt track topology of a single layer melt track produced by LAM of virgin Invar36 powder (B1) and (b) the third layer Invar36 melt track produced from LAM of oxidised powder (B2).